EFFECTS OF CONFINEMENT ON UNSTEADY TURBULENT SEPARATED FLOW OVER A GAUSSIAN BUMP

Adam Steacy[1], **Kevin H. Manohar**[2], **Robert J. Martinuzzi**[3], **Owen Williams**[2†], **and Chris Morton**[1†]
[1] Department of Mechanical Engineering, McMaster University, Hamilton, ON, Canada
[2] Department of Aeronautics and Astronautics, University of Washington, Seattle, WA, USA
[3] Department of Mechanical and Manufacturing Engineering, University of Calgary, Calgary, AB, Canada
[1]steacyr@mcmaster.ca, [2]kmanoh@uw.edu, [3]rmartinu@ucalgary.ca, [2†]ojhw@uw.edu, [1†]mortoc5@mcmaster.ca

ABSTRACT

The unsteady turbulent separated flow over a Gaussian bump is investigated experimentally in the University of Washington 3×3 Low-Speed Wind Tunnel to examine the influence of confinement on its unsteady dynamics. Four confinement levels are considered, from 13% up to 26% frontal area blockage based on the bump height ($h = 76.6$ mm), at a freestream velocity of $U_\infty = 45$ m/s ($Re_h \approx 2.26 \times 10^5$). Surface pressure measurements from an array of 32 taps are used to characterize the flow. Across all confinement levels, the flow exhibits a consistent set of frequencies at $St_h \sim 10^{-3}$ (1 Hz) and $St_h \sim 10^{-2}$ (13.5 Hz) associated with a large-scale spanwise motion of the separated region and a shear layer breathing motion, respectively. Increasing confinement does not introduce new modes, but amplifies this low-frequency component, leading to a redistribution of energy toward the dominant low-frequency global mode. As confinement increases, a transition to bimodal behaviour is observed, indicating the emergence of bistable switching between two antisymmetric states. Proper Orthogonal Decomposition (POD) identifies the leading mode as the primary indicator of the bistable dynamics, with its energy content increasing with confinement. The temporal coefficient of this mode evolves from Gaussian to bimodal distributions, providing a robust low-order indicator of state switching. Statistical analysis of the switching process reveals long dwell times ($tU_\infty/h \sim 10^3$) and log-normal dwell time distributions, consistent with stochastic transitions between metastable states. The findings highlight the importance of low-frequency unsteady dynamics in wall-mounted separated flows.

1 BACKGROUND AND MOTIVATION

Turbulent separated flows remain among the most challenging and practically significant problems in fluid mechanics. Flow separation is ubiquitous in many engineering applications, yet its accurate prediction remains an outstanding challenge. The NASA CFD Vision 2030 Study identifies the prediction of turbulent separated flows as one of the major challenges facing the field, noting that current time-averaged experimental results and Reynolds-Averaged Navier-Stokes (RANS) methods routinely fail to capture the unsteady dynamics and three-dimensional topology of separated wakes (Slotnick *et al.*, 2014).

Recent attention has shifted towards hills, bumps and ramp flows, which are characterized by their nominally symmetric and smooth geometries producing strong favourable pressure gradients (FPGs), adverse pressure gradients (APGs), separated wake, and three-dimensional flow topology (Wood, 1995). One relevant test geometry that has become a cornerstone in this research area is the Gaussian bump (Williams *et al.*, 2020). Designed to be a symmetric, wing-like aerodynamic surface, the speed bump generates a three-dimensional separated wake with several control parameters used to control the extent of flow separation (Gray *et al.*, 2021). It has a high aspect ratio ($w/h = 8.3$) allowing for interactions between different turbulent length scales.

Previous studies on bluff-body wakes and other bump flows have revealed the emergence of low-frequency unsteady dynamics. Notably, persistent downstream asymmetries in the wake have been found in the FAITH Hill (Bell *et al.*, 2012) as well as bistable switching modes in the BeVERLI hill (MacGregor & Lavoie, 2024) and the Ahmed body (Grandemange *et al.*, 2013). The bistable switching is characterized by the presence of large-scale coherent structures that dominate the flow field, resulting in reflective antisymmetric wake states (Volpe *et al.*, 2015). The switching between these states is stochastic and occurs over long timescales at $St_h \sim 10^{-3}$, alongside other low-frequency shear-layer motions at $St_h \sim 10^{-2}$. Similar timescales were observed in recent investigations of the Gaussian Bump (Manohar *et al.*, 2026), where global fluctuations in surface pressures were noted at $St_h \sim 10^{-3}$ in addition to shear layer breathing motions at $St_h \sim 10^{-2}$. Unlike the stochastic spanwise switching in the Ahmed and BeVERLI cases, the Gaussian Bump exhibited a global spanwise meandering defined by continuous lateral wake oscillation without long residence in a preferred state (Manohar *et al.*, 2026).

A recent review from Williams & Smits (2025) notes that these bistable switching modes are likely driven by the interaction of differently oriented shear layers at the edges of 3D geometries and that changing confinement is likely to alter these interactions. The transition between spanwise meandering and bistable behaviour has been previously linked to changes in orthogonal length scale interaction (Grandemange *et al.*, 2014). Further investigation of this low-frequency global mode is required when subjected to different boundary conditions and pressure gradients to alter the orthogonal shear layer interactions. The present work investigates the effects of increased confinement on the dynamics of the wake, with a specific aim to characterize any low-frequency behaviour (bistability or otherwise).

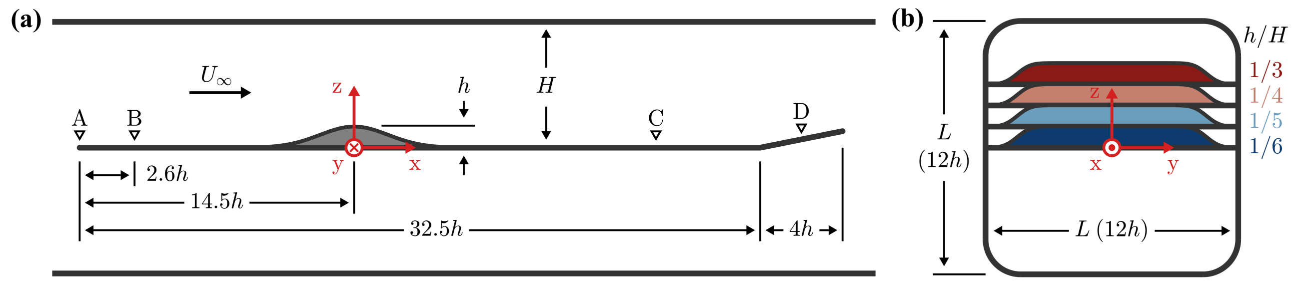

Figure 1. Cross-sectional schematic of the Gaussian bump mounted on the movable splitter plate in the UW 3×3 Low-Speed Wind Tunnel. (a) Side view showing the streamwise configuration with key dimensions annotated in bump heights, $h = 76.6mm$. The (A) super-ellipse leading edge, (B) 240-grit sandpaper trip strip location, (C) movable splitter plate, and (D) adjustable trailing edge flap are indicated. H denotes the splitter plate-to-ceiling distance. (b) Upstream cross-sectional view of the bump showing all four confinement levels, colour-coded by vertical confinement ratio, h/H.

2 FACILITIES AND EXPERIMENTAL SETUP

The experiments were conducted in the University of Washington's 3×3 Low-Speed Research Wind Tunnel at a nominal free-stream velocity of $U_\infty = 45m/s$ ($Re_h \approx 226,000$). This facility is equipped with an instrumented Gaussian Bump model, incorporating an array of surface pressure taps distributed along the streamwise and spanwise centerlines, with additional taps located within the downstream separated region (see Fig. 3(a)). The surface pressures are sampled at 12.5 kHz using AllSensors D1-4V-Mini analog differential sensors (F.S. ranges of 5, 10, or 20 inH_2O) connected to 24mm long tubes, digitized using an Advantech PCIe-1805 data acquisition card. All sensors reference a centerline splitter plate tap far upstream of the bump apex ($x/h = -10$), providing an adequate measure of the upstream static pressure (Williams *et al.*, 2020). Each acquisition was 30 minutes long, ensuring that a sufficient number of $St_h \sim 10^{-3}$ timescales were captured to achieve converged statistics.

The bump geometry, Williams *et al.* (2020), is scaled relative to the tunnel width, with a streamwise length and spanwise width of $L = 0.914m$ and bump height $h = 0.0766m$. The model is mounted to a movable splitter plate with a 10:1 modified super-ellipse leading edge that has static pressure taps on the top and bottom surfaces. The pressure difference across these taps was used to set the trailing edge flap for each confinement case such that the stagnation point lay slightly above the geometric leading edge (Williams *et al.*, 2020). The splitter plate develops a turbulent boundary layer using a one-inch wide strip of 240-grit sandpaper located 2.6h downstream of the splitter plate's leading edge. Tests are conducted at ($Re_h \approx 226,000$), ensuring that low Reynolds number effects such as relaminarization are not expected to be present.

The splitter plate-to-ceiling distance, H, enables the controlled variation of the vertical confinement ratio (h/H) and serves as a tuning parameter that directly influences the strength of the adverse pressure gradient. The test campaign examined four levels of confinement, with the two extreme cases used for detailed comparisons because of their distinctly different dynamics. The lowest confinement configuration (LC), mounted at $h/H = 1/6$, resulted in the lowest frontal area blockage ratio ($BR = 0.13$). The highest confinement configuration (HC), mounted at $h/H = 1/3$, resulted in the highest frontal area blockage ratio ($BR = 0.26$). Figure 1(b) provides schematics for all tested configurations. Previous experiments from Williams *et al.* (2020); Manohar *et al.* (2023) reported results for the lowest confinement level.

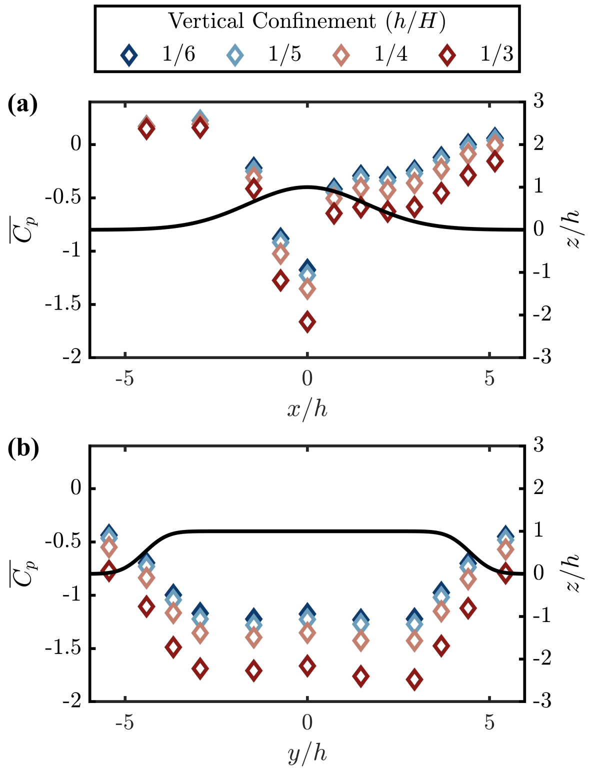

Figure 2. Mean surface pressure distributions for all four confinements at $Re_h \approx 226,000$. (a) Streamwise centerline plane at $y/h = 0$. (b) Spanwise centerline plane at $x/h = 0$.

3 RESULTS

3.1 Mean Flow and Spectra

The mean surface pressure distributions for both centerline planes of the bump are shown in Figure 2. Along the streamwise centerline (Fig. 2(a)), a monotonic decrease in surface pressure is observed with increasing vertical confinement, reflecting a strengthening of the adverse pressure gradient over the bump apex as the flow is increasingly accelerated between the bump and the tunnel ceiling. This is consistent with the expected acceleration of the freestream flow with increasing blockage ratio. Along the spanwise centerline (Fig. 2(b)), the pressure distributions remain symmetric about $y/h = 0$ across all confinement levels. Despite the nominally symmetric mean state, the instantaneous flow behaviour, discussed in the following sections, reveals strong asymmetric dynamics that are

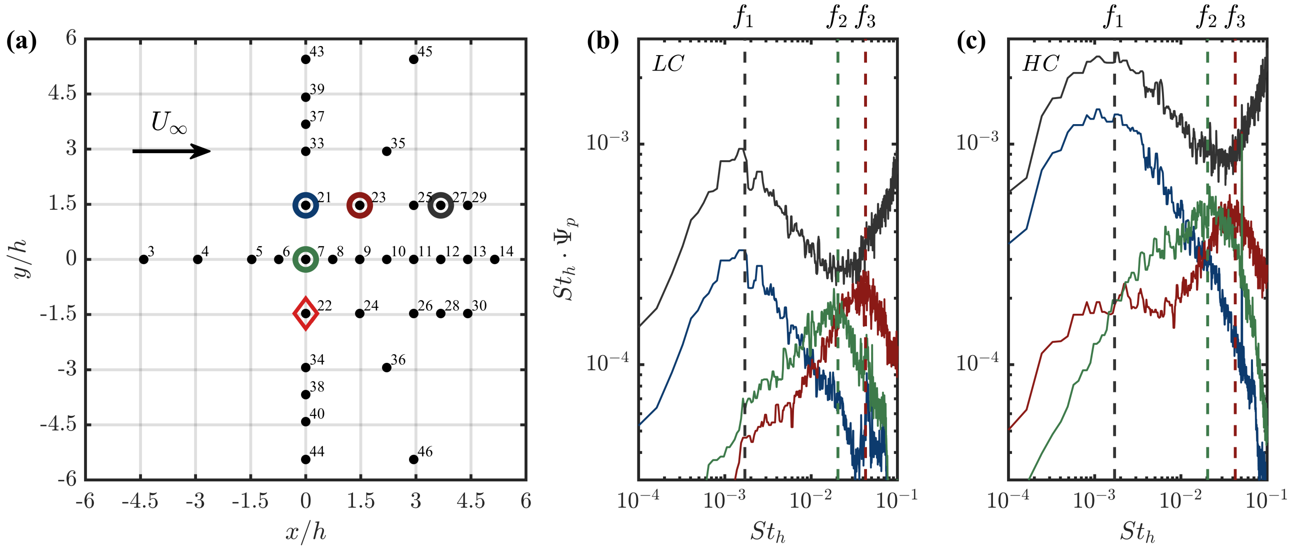

Figure 3. (a) Layout of the surface pressure tap array normalized by bump height, h, with taps used in subsequent spectral analysis highlighted with coloured circles. Premultiplied power spectral density functions ($St_h \cdot \Psi_p$) from unfiltered long-duration measurements are shown for the (b) lowest confinement, *LC*, and (c) highest confinement, *HC*, cases. Vertical dashed lines indicate characteristic frequencies: f_1 denotes $St_h \approx 1.7 \times 10^{-3}$ (1 Hz), f_2 denotes $St_h \approx 2.3 \times 10^{-2}$ (13.5 Hz), and f_3 denotes $St_h \approx 3.7 \times 10^{-2}$ (22 Hz).

entirely obscured by time-averaging.

The premultiplied power spectral density functions for key tap locations are shown in Figure 3(b) and (c) for the lowest and highest confinement cases, respectively. Across all confinement levels, three dominant frequencies are observed: a low-frequency peak at $St_h \approx 1.7 \times 10^{-3}$ (1 Hz), a shear-layer breathing mode at $St_h \approx 2.3 \times 10^{-2}$ (13.5 Hz), and signatures of surface vortices at $St_h \approx 3.7 \times 10^{-2}$ (22 Hz). The presence, spatial placement, and tap-to-tap variation of these frequencies are consistent with the detailed characterization reported by Manohar *et al.* (2026), who provide an extensive description of the spatial distribution of these modes. The low-frequency, 1 Hz component is detected most strongly at taps located near the edges of the separated region (Tap 27, black) and upstream along the apex (Tap 21, blue), but is notably absent in taps fully immersed in the mean separated region, indicating it is concentrated at the boundaries of the recirculation zone. The 13.5 Hz shear-layer breathing mode is localized near the centerline separation point, while the 22 Hz peak is confined to regions where surface vortices are expected to form.

Increasing confinement does not introduce new frequencies but instead redistributes energy across these existing modes. The low-frequency 1 Hz component grows in strength by nearly an order of magnitude with confinement, becoming broader and more energetic, while the higher-frequency components show comparatively minor changes (compare Fig. 3(b) and 3(c) for dominant frequency, f_1). This amplification of the low-frequency global mode is a key indicator of emerging bistable behaviour.

The pressure measurement time series shown in Figure 4 further highlights the effect of confinement on flow dynamics. In the low confinement case in Figure 4(a), pressure fluctuations remain small and approximately Gaussian, indicating a predominantly normal fluctuating turbulent field. In contrast, the highest confinement case in Figure 4(b) exhibits large-amplitude excursions from the mean that persist for $\sim 10^3$ convective time scales. These excursions are equal and opposite for symmetric tap pairs, meaning they likely represent large antisymmetric spanwise motions. These deviations produce bimodal probability distributions that are heavily biased towards one state with a roughly 75-25 split between peaks. The combination of bimodal surface pressure signals and a strong low-frequency peak suggests bistable switching behaviour. However, to confirm the presence of coherent large-scale structures governing these dynamics, further evidence is required.

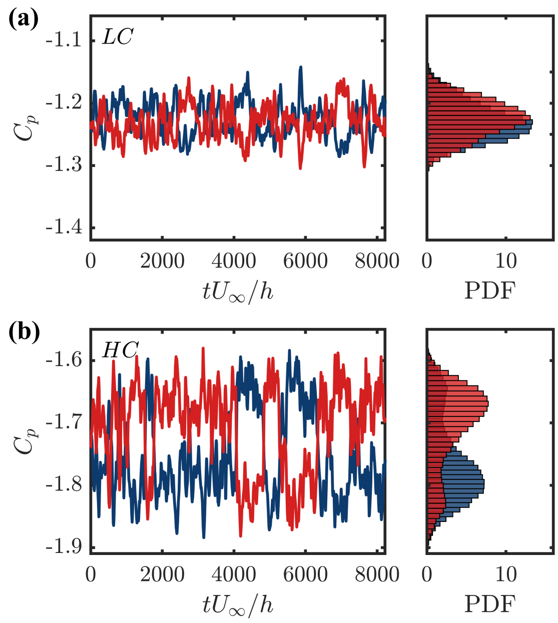

Figure 4. Time series of pressure measurements (Cp) from Tap 21 (blue) and Tap 22 (red, diamond marker in Fig. 3(a)) located immediately off centerline ($y/h = \pm 1.5$) on the bump apex ($x/h = 0$) for (a) lowest confinement, *LC*, and (b) highest confinement, *HC*, cases. Signals are low-pass filtered at 20 Hz to emphasize the low-frequency dynamics. Corresponding probability density functions of the full time series are shown on the right.

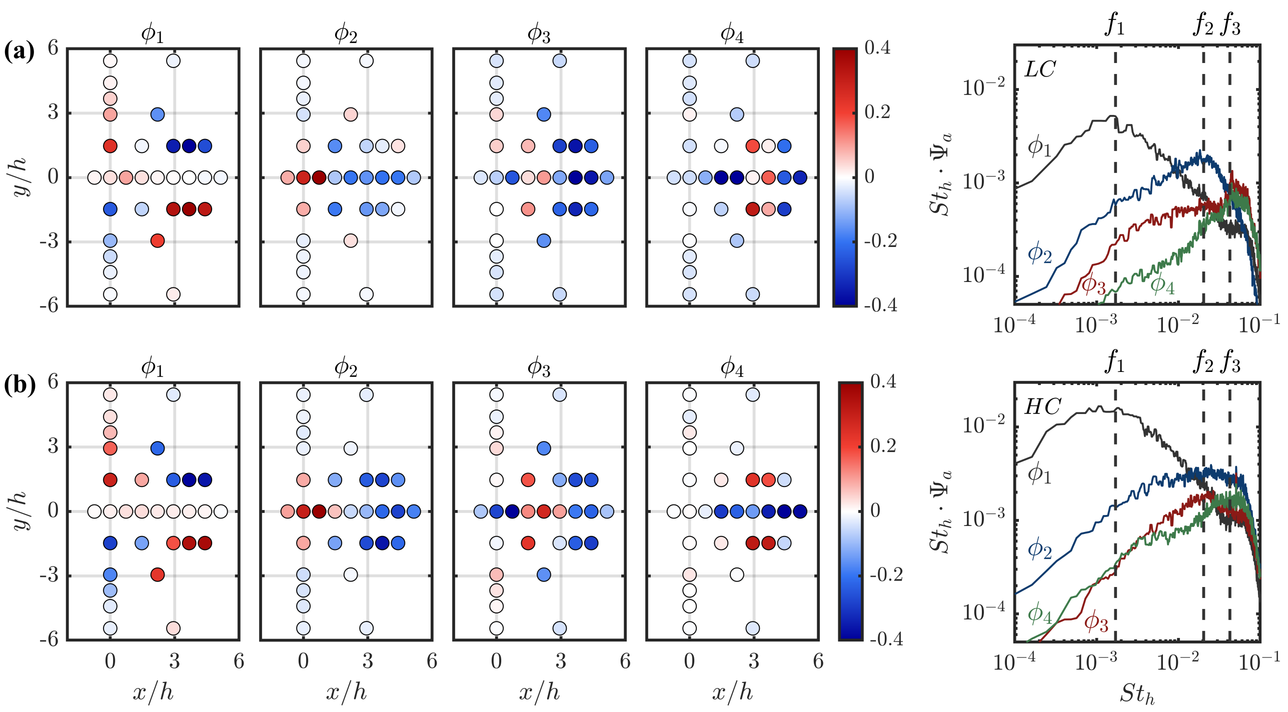

Figure 5. Spatial distributions of the first four POD modes (ϕ_1–ϕ_4), for the (a) lowest confinement, *LC*, and (b) highest confinement, *HC*, cases. The same colour scale is used for all modes. Premultiplied power spectral density functions of the temporal coefficients of the first four POD modes are shown alongside. Vertical dashed lines indicate characteristic frequencies: f_1 denotes $St_h \approx 1.7 \times 10^{-3}$ (1 Hz), f_2 denotes $St_h \approx 2.3 \times 10^{-2}$ (13.5 Hz), and f_3 denotes $St_h \approx 3.7 \times 10^{-2}$ (22 Hz).

3.2 Surface Pressure POD

Proper Orthogonal Decomposition (POD) of the surface pressure field was performed to extract the dominant coherent structures and their temporal behaviour. A 50 Hz low-pass filter was applied before decomposition to reduce the influence of the highly energetic shedding frequencies ($\sim$100 Hz) concentrated in downstream taps and focus on the low-frequency dynamics associated with the spanwise wake motions. The resulting spatial modes and their premultiplied temporal power spectra for the first four modes are presented in Figure 5 for both the lowest and highest confinement cases. Taken together, the spatial composition and spectral content of all four modes remain consistent across confinement levels.

Across all confinement levels, mode 1 (ϕ_1) exhibits a large-scale, antisymmetric pressure distribution that breaks spanwise symmetry. Its temporal coefficient is strongly peaked at $St_h \approx 1.7 \times 10^{-3}$ (1 Hz), confirming that ϕ_1 represents the low-frequency large-scale spanwise wake motions. The spatial structure and spectral content of this mode are consistent across confinement levels, reinforcing that the same underlying mechanism is active in all cases. Higher-order modes capture the previously identified $St_h \approx 2.3 \times 10^{-2}$ (13.5 Hz) and $St_h \approx 3.7 \times 10^{-2}$ (22 Hz) dynamics, corresponding to shear-layer breathing and surface vortices near the separation point, respectively. These higher-frequency spatial structures are largely consistent across confinement levels, indicating that confinement primarily changes the manifestation of the large-scale dynamics rather than altering local turbulence mechanisms. The primary differences are seen in the spectral energy, where Mode 1 shows a large increase in energy and peak width as confinement is increased, while a slight increase in the 13.5 Hz peak is observed in modes 3 and 4. This suggests an enhancement of the shear-layer breathing contribution as the adverse pressure gradient strengthens.

3.3 Emergence of Bistability

While the preceding analysis demonstrates that the dominant frequencies, spatial mode shapes, and relative modal energy distributions remain consistent across all confinement levels, a more subtle but fundamental change in the underlying flow dynamics emerges when examining the statistical behaviour of the POD temporal coefficients. Figure 6(a) shows the probability density functions of the normalized Mode 1 temporal coefficient across all four confinement levels. At the lowest confinement, the distribution is single-peaked and approximately Gaussian, indicative of a flow that fluctuates stochastically about a single preferred symmetric state. As confinement increases, this distribution progressively transitions to a distinctly bimodal distribution at the highest confinement level, indicating the emergence of two preferred asymmetric states between which the flow switches. This shift is accompanied by a redistribution of energy into the first POD mode, whose energy content rises from approximately 50% to 60% as shown in Figure 6(b).

Mode 1 retains the same global antisymmetric spatial structure across all confinement levels and contains the majority of the total flow energy. Thus, its temporal coefficient serves as a natural low-order parameter for tracking the instantaneous wake state, essentially capturing the large-scale spanwise position of the separated region. This allows the full pressure field time series to be segmented into two distinct states, enabling conditional averaging and targeted statistical analysis of each individual state independently. Figure 7(a) shows the probability density function of the full Mode 1 temporal coefficient time series for the highest confinement case, along with the conditionally segmented positive ($\mathscr{P}$) and negative ($\mathscr{N}$) states. The segmentation is performed by splitting the time series at sharp changes in the mean and then binning the segments using the threshold defined by the minimum prob-

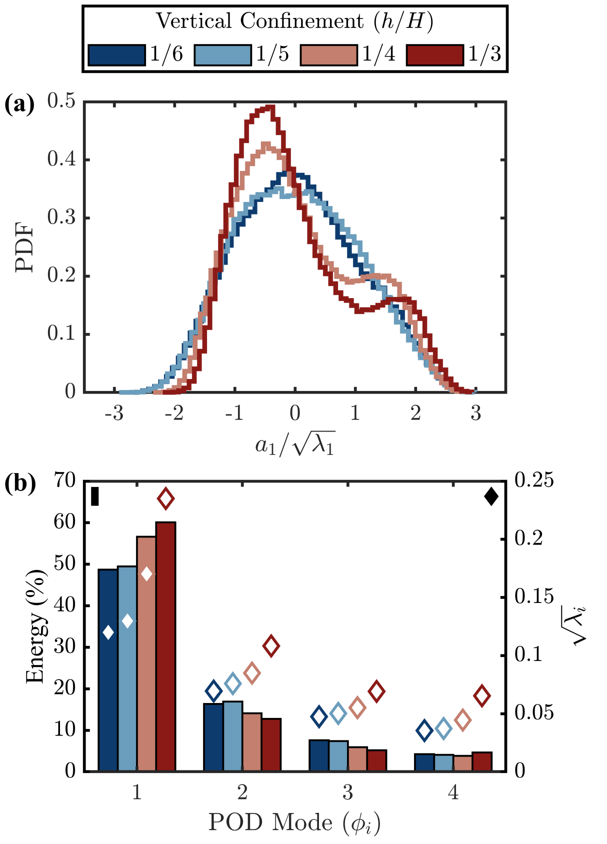

Figure 6. (a) Probability density functions (PDFs) of the normalized first POD mode temporal coefficient, $a_1/\sqrt{\lambda_1}$, for four confinement levels. (b) Modal energy content of the first four POD modes is shown as bars on the left axis, with the corresponding fluctuation amplitude, $\sqrt{\lambda_i}$, indicated by diamond markers on the right axis. Bars and markers are grouped by mode number with colours corresponding to the same confinement ratios shown in (a).

ability between the two bimodal peaks. The $\mathscr{N}$ state corresponds to a wake configuration in which the recirculation region is deflected toward the negative y/h side of the downstream separated region, with the $\mathscr{P}$ state representing the mirror-image configuration on the opposite side. The resulting state-conditioned signals are each independently Gaussian, indicating that each state corresponds to a distinct metastable attractor about which the flow fluctuates randomly. The system exhibits a 75-25 bias favouring the $\mathscr{N}$ state despite the nominally symmetric geometry. This asymmetric preference is consistent with bistable behaviour reported in other geometries, such as the Ahmed body (Plumejeau *et al.*, 2019) and BeVERLI hill (MacGregor & Lavoie, 2024), where similar occupancy biases have been attributed to the extreme sensitivity of the bistable dynamics to small changes ($< 1^\circ$) in yaw angle orientation.

Figure 7(b) shows the probability density function of the dwell times for the $\mathscr{N}$ state, plotted in convective timescales, with a log-normal fit corresponding to the mean and variance of the distribution. The dwell time distribution directly represents the time the flow spends in a given wake state between successive switching events, providing a statistical characterization of the switching process itself. The distribution follows a log-normal form with an average dwell time of $tU_\infty/h = 864$ $(1.47s)$, confirming that the flow remains locked in each state for extended periods before switching. This represents timescales that are orders of magnitude longer than the vortex shedding and shear-layer frequencies identified in the spectra. This provides evidence that the bistable switching is governed by a stochastic process rather than any periodic or deterministic forcing, consistent with classical descriptions of turbulence-driven transitions between metastable states (Volpe *et al.*, 2015).

The results collectively demonstrate that confinement does not alter the fundamental nature of the flow structures, but instead reorganizes how energy is distributed among them. Figure 6(b) shows that while Mode 1 consistently retains the majority of the total modal energy across all confinement levels, increasing confinement drives a redistribution of energy toward this dominant mode from the other higher-order modes. Alongside this redistribution, the net fluctuation amplitude ($\sqrt{\lambda_i}$) of each mode increases with confinement, indicating that the flow becomes more energetic overall as the adverse pressure gradient strengthens. This is consistent with a physical picture analogous to a double-well energy landscape, in which the flow occupies two symmetric metastable states separated by an energy barrier (Cadot *et al.*, 2015). At low confinement, the turbulent fluctuations are insufficient to overcome this barrier, and the flow continues to meander around a single symmetric state, producing the approximately single-peaked Gaussian statistics observed. As confinement increases and the overall fluctuation energy grows, the flow gains sufficient energy to regularly overcome the barrier and commit to one of the two antisymmetric states, producing the bimodal statistics and coherent long-lived switching behaviour characteristic of bistability. The stochastic nature of the switching that is confirmed by the dwell time analysis is entirely consistent with this picture of noise-driven transitions between two metastable attractors.

The broader implications of these findings are significant for both experimental and computational investigations of wall-mounted separated flows. The sensitivity of the bistable dynamics to confinement suggests that small variations in blockage ratio, tunnel geometry, or boundary conditions can fundamentally alter the observed flow behaviour. This provides a compelling explanation for variability in experimental observations of nominally identical geometries across different facilities. Critically, the nearly symmetric mean pressure distributions observed across all confinement levels demonstrate that time-averaged measurements alone are insufficient to characterize these dynamics, and that long-duration time-resolved measurements are essential. For computational campaigns, this highlights the danger of relying on steady or time-averaged metrics for validation of CFD models, where the true flow may be switching between strongly asymmetric states on timescales far exceeding typical simulation windows.

4 CONCLUSIONS

The present study provides a detailed statistical characterization of bistability in the separated flow over a high-aspect-ratio Gaussian bump and demonstrates the critical role of confinement in its emergence. The key findings of this study are as follows. A consistent set of dynamical frequencies is observed across all confinement levels with a low-frequency global mode at $St_h \sim 10^{-3}$ (1 Hz), a shear-layer breathing mode at $St_h \sim 2.3 \times 10^{-2}$ (13.5 Hz), and surface vortices at $St_h \sim 3.7 \times 10^{-2}$ (22 Hz). The characteristic frequencies, spatial pressure signatures, and relative modal energy distributions remain consistent for all modes across all confinement

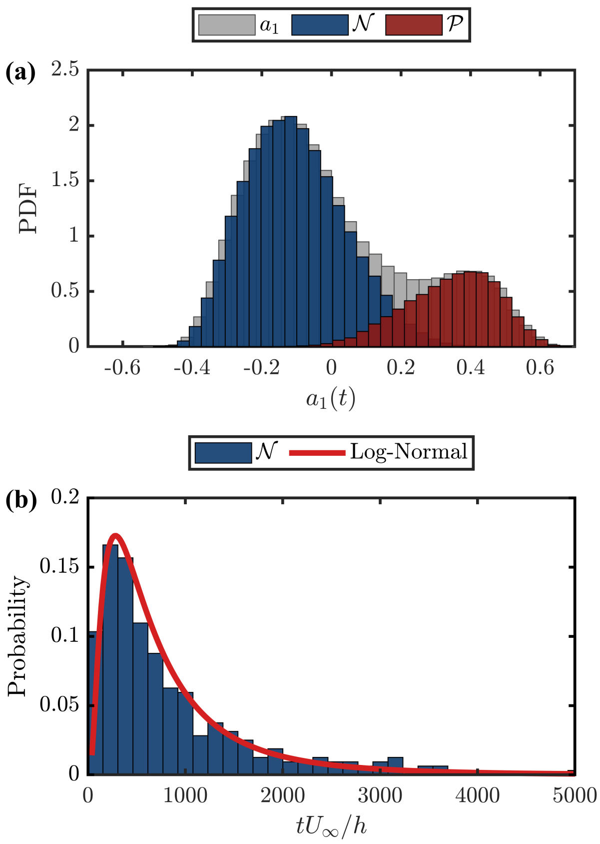

Figure 7. (a) Probability density function (PDF) of the first POD mode temporal coefficient, $a_1(t)$, for the highest confinement case, along with the conditionally segmented positive ($\mathscr{P}$) and negative ($\mathscr{N}$). (b) PDF of residence times for the $\mathscr{N}$ state signal, plotted in convective time, tU_∞/h, with a log-normal fit corresponding to the mean and variance of the distribution.

levels. This consistency strongly suggests that the same underlying physical mechanisms are active regardless of confinement level. However, confinement fundamentally changes how these mechanisms manifest. At low confinement, the flow is dominated by broadband turbulent fluctuations. In contrast, at high confinement, the energy redistributes toward the dominant low-frequency mode, driving a transition to coherent bistable switching between two metastable asymmetric states. The first POD mode serves as a robust low-order indicator of this transition, with its energy content rising from approximately 50% to 60% as confinement increases and its temporal coefficient evolving from a Gaussian to a distinctly bimodal distribution. A 75-25 bias between the $\mathscr{N}$ and $\mathscr{P}$ states highlights the sensitivity of this flow to small perturbations in boundary conditions and shows how difficult it is to characterize this behaviour from time-averaged measurements alone. Dwell time statistics follow a log-normal distribution, with an average dwell time of $tU_\infty/h = 864$ $(1.47s)$, confirming that the switching process is stochastic.

These findings carry implications for the broader study of wall-mounted separated flows and high-aspect-ratio bluff bodies. Bistability in this flow is not inherent to the bump geometry but an emergent behaviour that can be promoted or suppressed by modifying the streamwise pressure gradient through confinement, without any change to the bump geometry itself. This is a novel finding for the Gaussian bump and, more broadly, for high-aspect-ratio bump geometries, and suggests that confinement and pressure-gradient conditions are critical control parameters that must be carefully reported and controlled in both experimental and computational investigations of such flows. Ongoing PIV measurements synchronized with time-resolved surface pressures will further characterize the three-dimensional structure of each metastable state.

REFERENCES

Bell, J., Heineck, J., Zilliac, G., Mehta, R. & Long, K. 2012 Surface and Flow Field Measurements on the FAITH Hill Model. In *50th AIAA Aerosp. Sci. Meet. New Horiz. Forum Aerosp. Expo.*. Nashville, Tennessee: American Institute of Aeronautics and Astronautics.

Cadot, O., Evrard, A. & Pastur, L. 2015 Imperfect supercritical bifurcation in a three-dimensional turbulent wake. *Phys. Rev. E* **91** (6), 063005.

Grandemange, M., Gohlke, M. & Cadot, O. 2013 Turbulent wake past a three-dimensional blunt body. Part 1. Global modes and bi-stability. *J. Fluid Mech.* **722**, 51–84.

Grandemange, M., Gohlke, M. & Cadot, O. 2014 Turbulent wake past a three-dimensional blunt body. Part 2. Experimental sensitivity analysis. *J. Fluid Mech.* **752**, 439–461.

Gray, P. D., Gluzman, I., Thomas, F., Corke, T., Lakebrink, M. & Mejia, K. 2021 A New Validation Experiment for Smooth-Body Separation. In *AIAA Aviat. 2021 FORUM*. VIRTUAL EVENT: American Institute of Aeronautics and Astronautics.

MacGregor, D. & Lavoie, P. 2024 On The Structure and Behaviour of the Wake Behind a Three-Dimensional Hill. In *13th International Symposium on Turbulence and Shear Flow Phenomena (TSFP13)*.

Manohar, K. H., Annamalai, H., Williams, O., Morton, C. & Martinuzzi, R. J. 2026 Unsteadiness in turbulent separated flow over a three-dimensional Gaussian bump. *Journal of Fluid Mechanics* (under review).

Manohar, K. H., Williams, O. J., Martinuzzi, R. J. & Morton, C. 2023 Temporal super-resolution using smart sensors for turbulent separated flows. *Exp Fluids* **64** (5), 101.

Plumejeau, B., Delprat, S., Keirsbulck, L., Lippert, M. & Abassi, W. 2019 Ultra-local model-based control of the square-back Ahmed body wake flow. *Phys. Fluids* **31** (8), 085103.

Slotnick, J. P., Khodadoust, A., Alonso, J., Darmofal, D., Gropp, W., Lurie, Elizabeth & Mavriplis, D. J. 2014 CFD Vision 2030 Study: A Path to Revolutionary Computational Aerosciences. *Tech. Rep.* NF1676L-18332.

Volpe, R., Devinant, P. & Kourta, A. 2015 Experimental characterization of the unsteady natural wake of the full-scale square back Ahmed body: Flow bi-stability and spectral analysis. *Exp Fluids* **56** (5), 99.

Williams, O. J., Samuell, M., Sarwas, E. S., Robbins, M. & Ferrante, A. 2020 Experimental Study of a CFD Validation Test Case for Turbulent Separated Flows. In *AIAA Scitech 2020 Forum*. Orlando, FL: American Institute of Aeronautics and Astronautics.

Williams, O. J. & Smits, A. J. 2025 Asymmetries in Nominally Symmetric Flows. *Annu. Rev. Fluid Mech.* **57** (Volume 57, 2025), 35–60.

Wood, N. 1995 The onset of separation in neutral, turbulent flow over hills. *Boundary-Layer Meteorol* **76** (1), 137–164.